WILEY

IET The Institution of Engineering and Technology

ORIGINAL RESEARCH OPEN ACCESS

Design, Optimisation and Prototyping of Variable Reluctance Resolvers With Narrower Stator Excitation Teeth

Davood Karamalian[1,2] | Behrooz Majidi[1,2] | Mohammadreza Moradian[1,2] | Khoshnam Shojaei[1,3] | Sayyed Mohammad Mehdi Mirtalaei[1,2]

[1]Department of Electrical Engineering, Najafabad Branch, Islamic Azad University, Najafabad, Iran | [2]Smart Microgrid Research Center, Najafabad Branch, Islamic Azad University, Najafabad, Iran | [3]Digital Processing and MachineVision Research Center, Najafabad Branch, Islamic Azad University, Najafabad, Iran

Correspondence: Behrooz Majidi (Bmx@aut.ac.ir)

ABSTRACT

This paper aims to enhance the performance of the existing non-overlapping variable reluctance resolvers (VRRs) to obtain more accurate position signals by optimising the stator excitation teeth using genetic algorithm (GA). For this purpose, first, the principles of operation in non-overlapping VRRs are demonstrated using a magnetic equivalent circuit (MEC). Then, the MEC model is utilised to verify the principles of incorporating narrower excitation teeth in the non-overlapping model. The modified MEC provides a fast and sufficiently accurate model, so it is employed in the optimisation phase where GA is used to determine the optimal dimensions for the teeth. Following the MEC optimisation process, the proposed resolver is simulated and compared with a conventional equal teeth model using the finite element method (FEM). Finally, the proposed model with narrower excitation teeth is prototyped and tested. Results from MEC, FEM and the prototyped resolver confirm the effectiveness of the proposed model and validate the feasibility of using narrower excitation teeth to improve resolver's accuracy.

1 | Introduction

Rotor position is a key factor in coordinating servo motors in automation systems and controlling modern vehicles for less torque ripple and smoother performance [1]. Typically, position can be measured using either encoders or resolvers. Encoders are widely used across industries because of their acceptable accuracy, ease of manufacturing and simple signal processing. However, because encoders rely on optical methods for position detection, their performance degrades in harsh operating conditions such as mechanical vibration, humidity, noise, extreme temperatures and dust [2, 3]. In contrast, resolvers use magnetic fields for position detection, making them more robust in such challenging environments [4].

Resolvers can generally be classified into three types based on their configuration: wound rotor, variable reluctance rotor and printed circuit resolvers [5, 6]. All three types can be further categorised based on the direction of their magnetic field into axial, radial and linear types [7, 8]. Axial resolvers are commonly used in more electric aircraft and show higher fault tolerance under conditions such as eccentricity [9, 10]. However, the

complexity of rotor manufacturing, especially in high number of poles, limits their commercial application [11]. Linear resolvers are suitable for applications with linear motion [12].

Radial resolvers, because of their versatility, are the most commonly used type across industries. In wound rotor resolvers (WRRs), the excitation winding is placed on the rotor and fed by a rotary transformer (RT) or a set of slip rings (SR) and commutators. The use of RTs and SRs increases the likelihood of faults due to wear over time [13]. Additionally, the manufacturing and maintenance of the tertiary winding are intricate. PCB resolvers, on the other hand, benefit from simple configuration but perform poorly in the presence of electromagnetic harmonics. Nevertheless, variable reluctance resolvers (VRRs), with their solid, winding-less and without RTs rotor are thinner and easier to manufacture than their WR counterparts. However, placing two signal coils and an excitation coil on each stator tooth creates issues like lack of winding space, stator asymmetry, coil damage and winding complexity.

To overcome these challenges, a non-overlapping winding model was introduced in Refs. [14, 15]. This winding method offers two key advantages. First, each stator tooth is dedicated to a single coil, separating the signal coils from the excitation coil. This leads to higher accuracy, simpler winding and more space for each coil. Second, both the excitation and signal coils have a constant number of turns. This winding model can be applied to different combinations of stator/rotor pole pairs. A higher number of rotor poles increases accuracy, whereas fewer poles are better suited for high-speed applications. Among the possible combinations, the 12/5-X configuration is the most commercially viable, offering a balance between accuracy and speed. As a result, the non-overlapping 12/5-X VRR configuration has gained significant attention in different literatures.

Some studies focused on optimising the winding, comparing different winding diagrams and methods for non-overlapping winding mathematically [16–18]. In Ref. [19], an outer rotor configuration with non-overlapping winding is proposed and investigated, using the same 12/5-X combination that demonstrated accurate position detection. In Ref. [20, 21], a permanent magnet (PM) model based on this concept is introduced, where the signal windings are replaced by Hall sensors and the excitation coils are replaced by PMs. This PM model performs better in high-speed applications because of DC excitation. A slot-less PM resolver is presented in Ref. [22], simplifying the manufacturing process. Some studies focused on rotor optimisation. In Ref. [23], the rotor contour is optimised to minimise position error by adjusting the air gap reluctance.

Among all the models presented, however, the shape of the stator was never investigated closely. In previous studies, slot-opening width was the primary parameter used to represent the teeth with all excitation and signal teeth considered to be equal. As a result, with changing one parameter, the best dimension was found. There are, however, several stator configuration optimisation methods used in electrical machines that could be adapted for VRRs. Unequal teeth configuration (UNET) has been applied to create more desirable flux paths in machines with asymmetric stator teeth [24–26]. In Ref. [24], the

non-overlapping winding is applied on a permanent magnet synchronous machine and analytical method was employed to predict and understand the back-EMF behaviour. In Ref. [25], the same approach was employed to optimise unequal teeth segmented permanent magnet machines. In Ref. [26], the analytical approach is used in unequal teeth structure to reduce electromagnetic vibration in Vernier machines. To the best knowledge of the authors, this method was never used for resolvers. Therefore, the following steps are taken in this paper for the stator optimisation:

- The principles of using UNET configuration in resolvers and its effectiveness are investigated by MEC and flux lines plot.

- Rather than using the slot opening parameter, two parameters are used to optimise excitation teeth.

- Excitation and signal teeth are optimised separately.

In the optimisation phase, all the aforementioned studies used either MEC or FEM for their optimisations. Several studies have focused specifically on MEC models for VRRs. In Ref. [27, 28], an accurate MEC is represented with much faster simulation time and acceptable accuracy. This model is expanded for eccentricity analysis and nonlinearity modelling [29]. The authors in Ref. [30] used Schwarz–Christoffel mapping to map the teeth in MEC models. In this paper, a modified MEC model for accurate teeth demonstration is needed and represented. The MEC model is chosen to enable fast evaluation and simulation of the model. This facilitates performing a higher number of iterations in a shorter time. The MEC modifications are as follows:

- Every tooth is modelled with three flux paths rather than one.

- The reluctance of each tooth is represented by six segments.

- Genetic algorithm (GA) is employed to optimise the segments of each tooth.

However, FEM can simulate the model with high accuracy. Therefore, after analysing the model using MEC, the results were also verified using FEM to validate the effectiveness of the proposed model. This paper follows this outline: first, the possibility of creating a resolver with unequal teeth with MEC model of the proposed resolver is presented to study the effects of unequal teeth on flux distribution and inductances. Afterward, modified MEC model is represented, and optimisation variables are formulated mathematically. Then, GA is used to carry the optimisation and find the best solution. Then, the optimal configuration is simulated using FEM to ensure the effectiveness of the proposed resolver, and finally, the results are verified by experimental tests.

2 | Principles of Studied Unequal Teeth Non-overlapping Resolvers

Variable reluctance resolvers (VRRs), like any other machine topology, consist of a rotor and a stator. The rotor is a solid
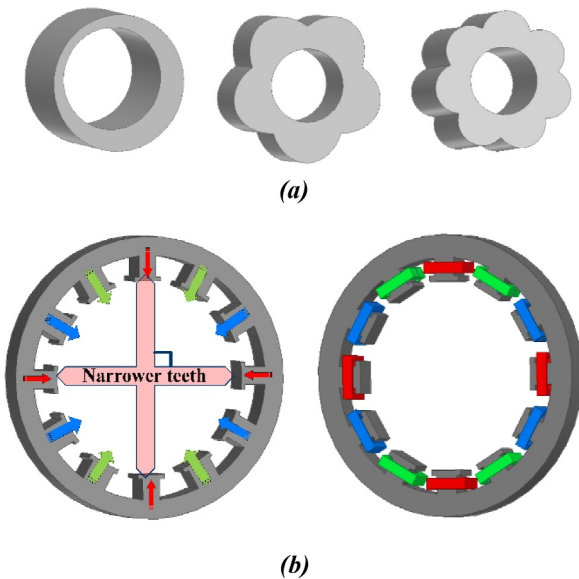
symmetric ferromagnetic component mounted on the shaft, synchronizing it with the main machine. Rotor has a unique salient sinusoidal shape and can be manufactured with different poles such as (1,5,7)-X shapes. This sinusoidal shape generates a variable magnetic field in the air gap. The rotor can be expressed as Equation (1) and shown in Figure 1a.

$$\delta = \frac{\alpha}{\beta + \cos(p\theta)} \tag{1}$$

where α is the length factor, β represent the shape factor, p is number of pole pairs and θ is the rotor angle. The value for α and β are chosen 1.3 and 1.5, respectively, according to [15]. The stator is composed of laminated ferromagnetic layers and windings. The stator used in this paper has 12 slots but a different number of slots can also be utilised. In 12-slots configuration, 4 slots of the stator are assigned for the excitation and remained 8 slots are divided to sine and cosine signal windings. The key difference between the proposed UNET configuration and the conventional one is the size of the excitation teeth. As it is shown in Figure 1b, the proposed UNET VRR has narrower excitation teeth, whereas in the conventional one, all teeth are equal. The winding method employed is non-overlapping with the same number of turns for signal coils and excitation [15]. Signal coils consist of two separate electrically perpendicular sine and cosine coils and their directions are shown in Figure 1b. The same winding method is also utilised for the proposed UNET configuration.

The excitation coil is fed by a high-frequency (HF) source as represented in Equation (2) which creates variable air gap flux between the stator and the rotor.

$$V_{Ex} = V_m \sin(\omega t + \varphi) \tag{2}$$

where V_{Ex} is the amplitude of excitation voltage and ω is the angular frequency. Figure 2 shows the excitation signal used to feed the resolver.

The variations in flux are directly related to the rotor's geometry and saliencies, leading to changes in the magnetic field within the two perpendicular signal windings. This orthogonality generates two perpendicular signals with different values at every position of rotor position, which can be calculated using Equations (3) and (4):

$$V_{\cos} = AN_{sig}\omega_m \, cos(P\theta)\sin(\omega t + \varphi) \tag{3}$$

$$V_{\sin} = AN_{sig}\omega_m \, sin(P\theta)cos(\omega t + \varphi) \tag{4}$$

where V_m, $V_{\cos}$ and $V_{\sin}$ represents the maximum voltage of the excitation coil, cosine and sine voltages, respectively. A is the air gap flux created by the excitation coil, N_{sig} is the number of turns in the signal coils and φ is phase shift between excitation and signal windings. In the next step, using Hilbert transformation the value of the envelope function of Equations (3) and (4) are expressed by Equations (5) and (6).

$$V_{\cos}^{En} = AN_{sig}\omega_m \cos(P\theta) \tag{5}$$

$$V_{\sin}^{En} = AN_{sig}\omega_m \sin(P\theta) \tag{6}$$

$V_{\cos}^{En}$ and $V_{\sin}^{En}$ represent outputs of the Hilbert function. Rotor position can be extracted using inverse tangent as Equation (7).
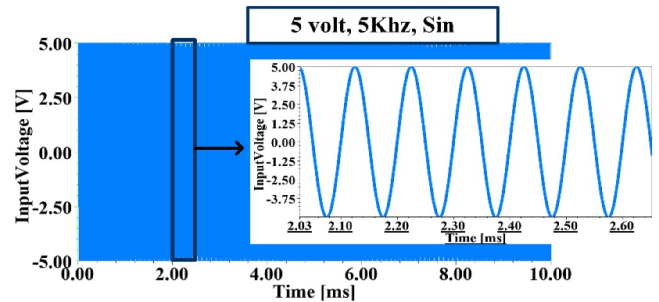
$$\theta = \text{Arctan} \frac{V_{\cos}^{En}}{V_{\sin}^{En}} \tag{7}$$

The flowchart for the operation of the resolver and computation of the position is shown in Figure 3 and the geometrical and electrical parameters of the studied resolver are given in Table 1.
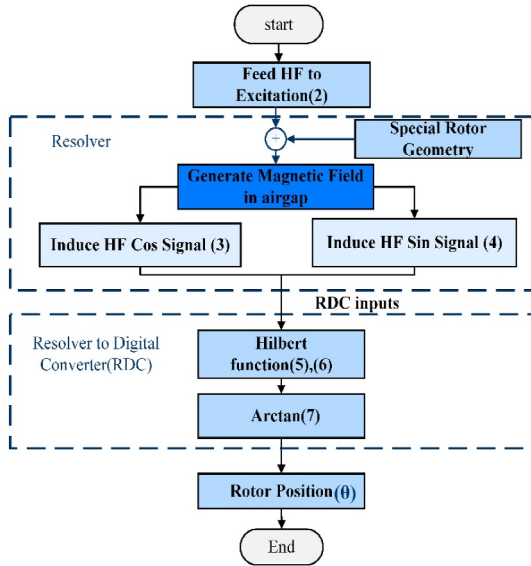
Two indicators, maximum position error (MPE) and average absolute position error (AAPE), are widely used for the comparison between resolvers and can be calculated using Equations (8) and (9).

$$AAPE = \frac{1}{N} \sum_{i=1}^{N} \left| \theta_{\text{actual},i} - \theta_{\text{measured},i} \right| \tag{8}$$

$$MPE = \max |\theta_{\text{actual}} - \theta_{\text{measured}}| \tag{9}$$

FIGURE 1 | Conventional and proposed variable reluctance resolvers with non-overlapping winding. (a) 1-X, 5-X and 7-X rotor configuration. (b) Stator of the proposed and conventional VRR.

FIGURE 2 | Excitation signal given to excitation signals.

FIGURE 3 | Flowchart of calculating position.

TABLE 1 | Resolver's geometrical and electrical parameters.

Stator/Rotor parameters	
Stator outer diameter	37 mm
Stator inner diameter	26 mm
Yoke diameter	2.5 mm
Stator/rotor poles	12/5 poles
Max/Min rotor diameter	25.4/24 mm
Rotor shaft diameter	12 mm
Stack length	8 mm
Excitation parameters	
Excitation frequency	5 kHz
Excitation voltage	5 volts
Excitation coil turns	70 turns
Signal coil turns	70 turns
Winding model	Non-overlapping

3 | The Effects of Utilising UNET

This section outlines the principles for the proposed UNET resolver and compares the proposed model with the conventional model by a simplified MEC model. According to Figure 1, every stator can be divided to 4 identical quadrants with one excitation tooth and two signals. VRRs can be ideally represented by self and mutual inductances using Equation (10).

$$\begin{bmatrix} \lambda_{Ex} \\ \lambda_C \\ \lambda_S \end{bmatrix} = \begin{bmatrix} L_{Ex}(\theta) & M_{Ex,C}(\theta) & M_{Ex,S}(\theta) \\ M_{C,Ex}(\theta) & L_C(\theta) & M_{C,S}(\theta) \\ M_{S,Ex}(\theta) & M_{S,C}(\theta) & L_S(\theta) \end{bmatrix} * \begin{bmatrix} i_{Ex} \\ i_C \\ i_S \end{bmatrix} \quad (10)$$

where λ, i, L and M are linkage flux, current, self-inductance and mutual inductance, respectively. The signal coils in the resolver are connected to a RDC with a very high resistance, resulting in $i_c = i_s = 0$. Therefore, Equation (10) can be simplified as Equation (11):

$$\begin{cases} \lambda_{Ex} = L_{Ex}(\theta).i_{Ex} \\ \lambda_c = M_{c,Ex}(\theta).i_c \\ \lambda_S = M_{S,Ex(\theta)}.i_S \end{cases} \quad (11)$$

In practice, based on Figure 4a,b, where only one excitation pole is fed by a HF signal, the quadrants are not separated magnetically, and there is a mutual flux between two subsequent excitation poles. Therefore, a more accurate matrix can be expressed as Equation (12) where the mutual fluxes between all teeth are considered. The whole flux lines, when all four excitation teeth are fed, are also shown in Figure 4c.

$$\begin{bmatrix} L_{Ex1} & M_{1,2} & M_{1,3} & & \boldsymbol{M_{Ex1,Ex10}} & \boldsymbol{M_{1,11}} & \boldsymbol{M_{1,12}} \\ M_{2,1} & L_{C2} & M_{2,3} & \cdots & \boldsymbol{M_{2,10}} & \boldsymbol{M_{2,11}} & \boldsymbol{M_{2,12}} \\ M_{3,1} & M_{3,2} & L_{S3} & & \boldsymbol{M_{3,10}} & \boldsymbol{M_{3,11}} & \boldsymbol{M_{3,12}} \\ & \vdots & & \ddots & & \vdots & \\ \boldsymbol{M_{10,1}} & \boldsymbol{M_{10,2}} & \boldsymbol{M_{10,3}} & & L_{Ex10} & M_{Ex,S} & M_{Ex,S} \\ \boldsymbol{M_{11,1}} & \boldsymbol{M_{Ex,S}} & \boldsymbol{M_{Ex,S}} & \cdots & M_{Ex,S} & L_{C11} & M_{Ex,S} \\ \boldsymbol{M_{12,1}} & \boldsymbol{M_{Ex,S}} & \boldsymbol{M_{Ex,S}} & & M_{Ex,S} & M_{Ex,S} & L_{S12} \end{bmatrix} \quad (12)$$

Mutual inductance between two excitation poles can be written as Equation (13).

$$M = \frac{\mu\,N^2 S}{L} \quad (13)$$

where M is mutual inductance, μ is permeability, N is number of turns, S is area and L is distance between two coils. According to Equation (13), narrowing the width of the excitation teeth increases the length L which in turn leads to a decrease in the mutual inductance M. Therefore, the arrays shown in red in Equation (12) are affected by narrowing the excitation teeth resulting in more ideal-like resolver in which more flux passes through signal windings.

4 | MEC Analysis of the Proposed Resolver

The MEC model for the proposed UNET configuration is represented in Figure 5. In this model $2N_s$ flux passes are used to accurately model the resolver. Every flux path reluctance is shown by Ri_j where i is the number of zone and j is the number of node where the path is located.

4.1 | Mathematical Model

According to this model, following Equations (14)–(21) Kirchhoff's circuit laws (KVLs and KCLs) can be applied to obtain magnetic equations.
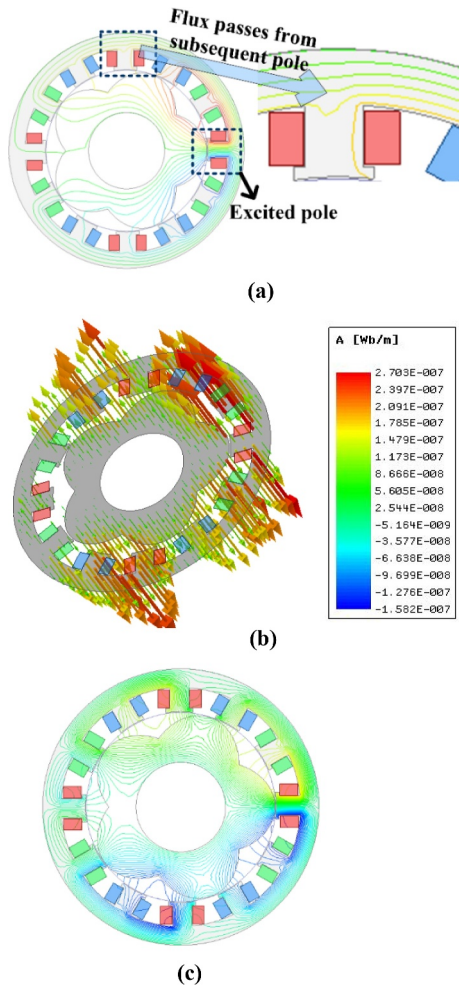
Stator equations are given as follows:

$$[R_s].[\gamma_s] = 0 \quad (14)$$

where

$$[R_s] = \begin{bmatrix} R1_i & -R2_i & R2_{i+1} & -R3_i & 0 & 0 & 1 & 0 \\ 0 & 0 & 0 & R3_i & -R4_i & R4_{i+1} & 1 & -R5_i \end{bmatrix} \quad (15)$$

(a)

(b)

(c)

FIGURE 4 | Flux analysis for VRRs. (a) Flux between two excitation poles when only one tooth is excited. (b) Flux vectors with only one tooth being excited. (c) Flux lines in a fully excited resolver.

$$[\gamma_s] = \begin{bmatrix} \varphi 1_i & \varphi 2_i & \varphi 2_{i+1} & \varphi 3_i & \varphi 4_i & R4_{i+1} & f & \varphi 5_i \end{bmatrix}^T \quad (16)$$

Airgap equation is given as follows:

$$\begin{bmatrix} R5_i & 0 \\ 0 & 1 \end{bmatrix} \begin{bmatrix} \varphi 5_i \\ \varphi 6_{i+1} \end{bmatrix} + \begin{bmatrix} -1 & -1 \\ 0 & -\sum_{k=1}^{24} G(U_i, U_{i+1}) \end{bmatrix} \begin{bmatrix} U_i \\ U_{i+1} \end{bmatrix} = 0 \quad (17)$$

Rotor equations are given as follows:

$$[R_r] [\varphi_r] + [B][U] = 0 \quad (18)$$

where

$$[R_r] = \begin{bmatrix} -R6_i & R6_{i+1} & R7_i & 0 & 0 & 0 \\ 0 & 0 & -R7_i & R8_i & -R8_{i+1} & R9_i \end{bmatrix} \quad (19)$$

$$[\varphi_r] = \begin{bmatrix} \varphi 6_i & \varphi 6_{i+1} & \varphi 7_i & \varphi 8_i & \varphi 8_{i+1} & \varphi 9_i \end{bmatrix}^T \quad (20)$$

$$[B][U] = \begin{bmatrix} -1 & -1 \\ 0 & 0 \end{bmatrix} \begin{bmatrix} U_i \\ U_{i+1} \end{bmatrix} \quad (21)$$

where φi_j is the flux for Ri_j, f is magnetomotive force of excitation teeth, U_i is the potential of ith node and G represents the gap function. It is worth mentioning that the number of zones and nodes can be changed to obtain desirable accuracy. By adding exciting according to Equation (2), electrical equation can be written as Equation (22):

$$v_{Ex} - r i_{Ex} = \frac{d\lambda_{Ex}}{dt} \quad (22)$$

To solve Equation (22), different numerical methods can be used and Euler method is used in this paper based on Equation (23).
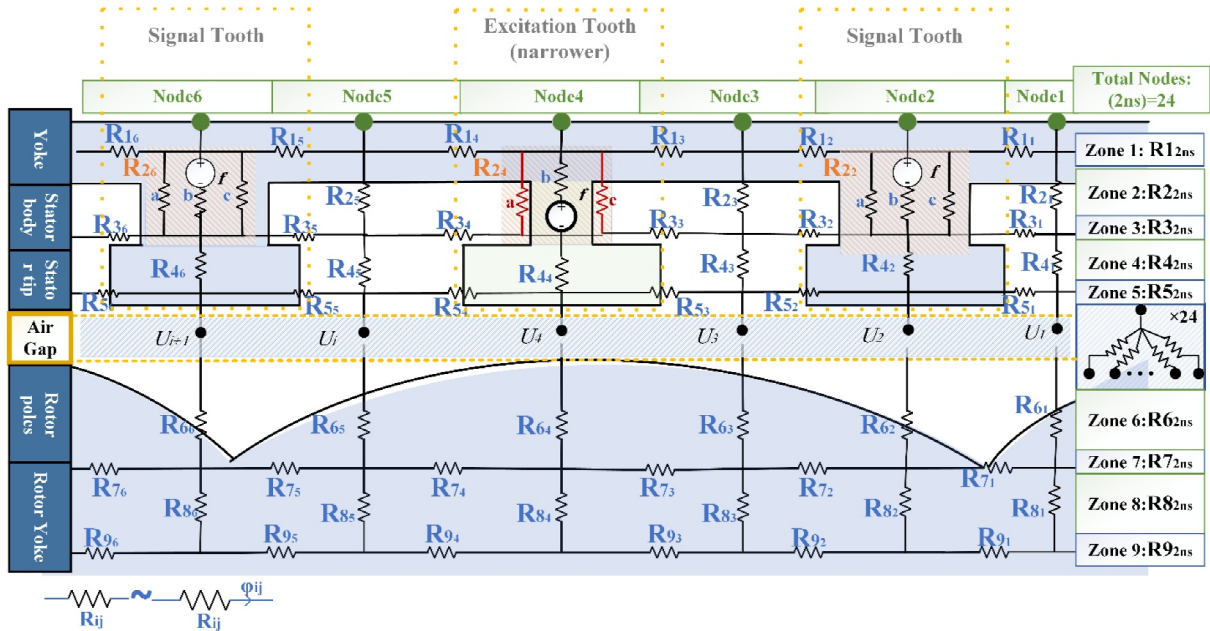
FIGURE 5 | MEC model for excitation and signal windings.

$$v_{Ex}^k - r i_{Ex}^k = \frac{\lambda_{Ex}^{k+1} - \lambda_{Ex}^k}{\Delta t} \;\rightarrow\; \lambda_{Ex}^{k+1} = \lambda_{Ex}^k + \Delta t\left(v_{Ex}^k - r i_{Ex}^k\right) \quad (23)$$

where Δt is the MEC step time and should be small enough to yield accurate results. As it is shown in Figure 5, the middle tooth (Node4) is narrower than other two signal coils. The flux tube in excitation teeth is described in more accurate model by three reluctances for the further optimisation. Therefore, the equivalent reluctance for each excitation tooth is described as Equation (24).

$$R2_{3n-2} = \left(\frac{1}{R_a} + \frac{1}{R_b} + \frac{1}{R_c}\right)^{-1} \quad (24)$$

in which R_a, R_b and R_c are three reluctances in parallel. 3n-2 term is specifying the excitation teeth.

4.2 | Stator Teeth Optimisation

In order to optimise the dimensions of the proposed resolver, a parametric model for excitation and signal teeth is required. The dimensions of the resolver can be expressed with the

iron segment of the teeth decreases and narrower teeth is achieved. Teeth saturation based on the B–H curve for steel-1010 limits the minimum of a.

According to Figure 6, reluctance for different parts can be modified as Equations (25)–(30):

$$R_{S1} = \frac{w_{\text{body}}}{\mu(i) * \left(h_{\text{tip}} * l_s\right)} \quad (25)$$

$$R_{s2} = \frac{h_{\text{body}}}{\mu(i) * \left(w_{\text{body}} * l_s\right)} \quad (26)$$

$$R_{s3,4} = \frac{w_{\text{tip}}}{\mu(i) * \left(h_{\text{tip}} * l_s\right)} \quad (27)$$

$$R_{s7} = \frac{h_{\text{yoke}}}{\mu(i) * \left(\frac{2\pi}{N_s} * l_s\right)} \quad (28)$$

$$R_{\text{air}} = \frac{h_{\text{tip}}}{\mu(\text{air}) * \left(\frac{2\pi}{N_s} - w_{\text{body}} - 2w_{\text{tip}}\right) * l_s} \quad (29)$$

$$R_{s5,6} = \begin{cases} \dfrac{h_{\text{body}}}{\mu(i) * (a * l_s)} + \dfrac{h_{\text{body}}}{\mu(\text{air}) * (w_{\text{tip}} - a) * l_s} & N \in 3n - 2 \text{ (narrower teeth)} \\[3mm] \dfrac{h_{\text{body}}}{\mu(i) * \left(0.8 w_{\text{tip}} * l_s\right)} + \dfrac{h_{\text{body}}}{\mu(\text{air}) * \left(0.2 w_{\text{tip}} * l_s\right)} & N \notin 3n - 2 \text{(signal teeth)} \end{cases} \quad (30)$$

defining separate segments for excitation and signal teeth shown in Figure 6. Yoke and segments (S1–S4) are chosen iron and are the same size for both signal and excitation teeth. However, segments (S5–S6) undergo the optimisation. In this optimisation, the parameter a changes, and the error is calculated based on Figure 3. By increasing the value of a, the
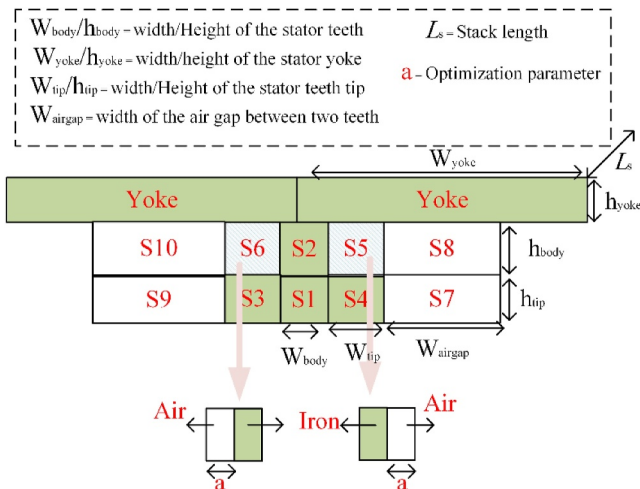

**FIGURE 6** | Excitation teeth segments for the optimisation.

Reluctances Equations (25)–(29) represent constant reluctances for every tooth, defined by the initial geometrical parameters provided in Table 1. In Equation (30), two terms are defined for the excitation and signal teeth. The first term represents the geometry of the narrower excitation teeth (teeth numbers 2, 5, 8 and 11), whereas the second term corresponds to the signal teeth. By replacing the stator teeth dimensions into the MEC equations, the following equation can be calculated:

$$\varphi = [f_s] * [z]^{-1} \quad (31)$$

where z is impedance matrix. The excitation winding is fed by Figure 2 and represented by f. φ is the flux passes through each signal winding.

4.3 | Optimisation Algorithm

Based on the mathematical model of the teeth in the MEC model, different algorithms can be utilised in the optimisation stage. Among all, genetic algorithm (GA) shows accurate modelling in machine design. GA is applied and the optimisation is based on Figure 7. Results of the GA optimisation are presented in Figure 7. Based on the principles of GA in Figure 7b in every iteration,
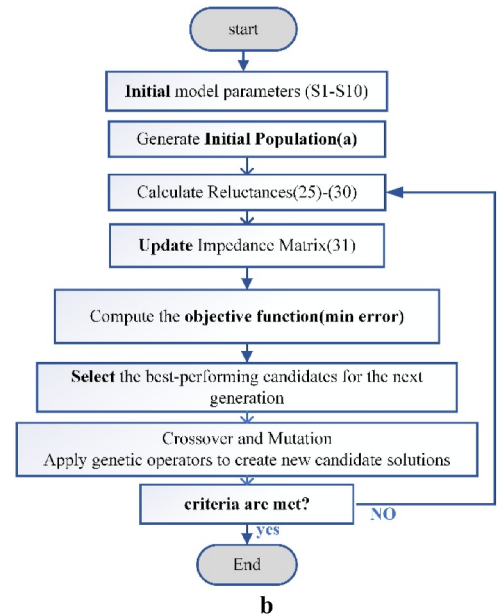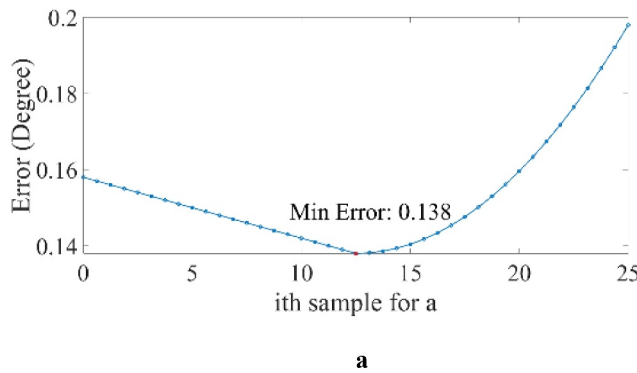
FIGURE 7 | GA used for the stator teeth optimisation and the results. (a) GA output for every iteration. (b) Applying GA to the MEC model.

impedance matrix is changed based on the reluctances obtained from Equations (25)–(30).

According to Figure 7, the lowest error occurred in $a = 0.127$ mm and larger values for a saturated the resolver which resulted in higher error. The proposed model with the optimised excitation teeth is then simulated, and Figure 8a represents the sine and cosine signals and the correspondent envelopes. Figure 8b shows the THD value of the proposed optimised model and conventional model and harmonic content of both models.

In order to obtain the envelope of the signals, high frequency signals should be demodulated. Hilbert function is used to filter the high frequency and extract the envelope of the signal.

5 | FEM Analysis of Proposed Resolver and Comparison

FEM-based simulation is another powerful tool for optimisation. Various software packages provide FEM analysis and help simulate and check the results of MEC. However, FEM simulations can be time consuming, especially when combined with GA optimisation that involves large population sizes and many iterations, leading to significant CPU demand; but with defining stator poles in cylindrical reference and expressing excitation pole length in degrees with limited number of samples, the accuracy of results can be checked.
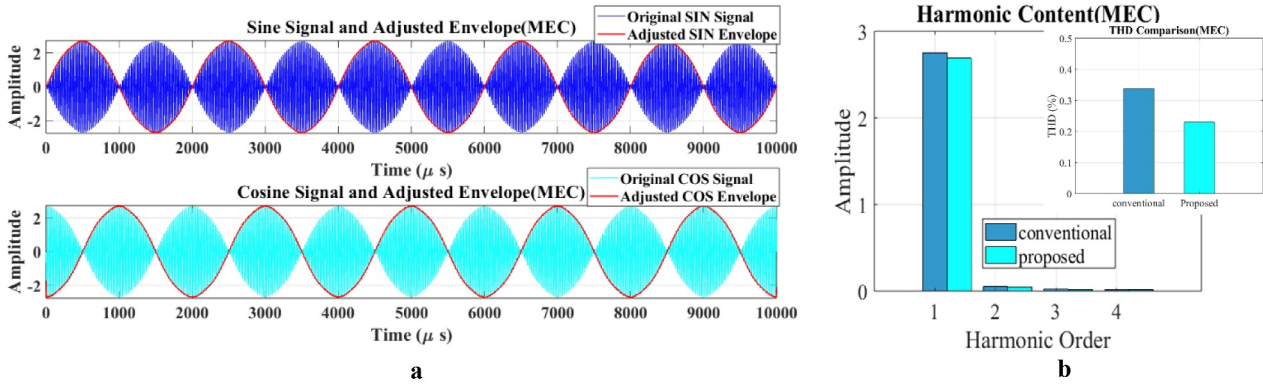
5.1 | FEM Optimisation

By defining a variable parameter (X) for the teeth length, the excitation tooth width can be adjusted by changing X from 12° to 26° in 2° increments. The minimum angle of 12° is selected based on the smallest tooth size before the resolver reaches

saturation, whereas the maximum angle of 26° represents the largest tooth pitch where signals from two signal poles intersect. In order to obtain the optimal value of this parameter, the simulation is performed using sensitivity analysis by defining the size parameters in the resolver in Maxwell software. The same approach is applied for the signal windings. In this case, to optimise the signal poles, the parameter (Y) was chosen for the optimisation. Therefore, the angle of the stator can be changed between 12° and 26° with 2° step. The results are shown in Figure 9. The comparison between MEC simulation and the FEM is shown in Table 2.

In the proposed model, an angle of 20° for the signal poles and 14° for the excitation poles results in the least error. Figure 10 shows the schematic of the optimised UNET resolver. To enable fair comparison, all fundamental parameters—such as the excitation signal values, number of windings turns and input waveform—are kept identical to the conventional resolver model. Additionally, the winding model, mesh settings and time step used in the simulation are the same for both models. Based on the flux distribution analysis, the flux lines in the proposed resolver pass through the signal coils more effectively than in the conventional model. Although there is nearly zero flux under the horizontal excitation poles in the UNET configuration, the conventional model exhibits uniform flux distribution under all four poles. This leads to less mutual effects between excitation coils which is obtained by narrowing the excitation teeth. The magnetic flux density (B) distribution for the proposed UNET is also presented in which the same zones with less flux lines have less density. The mesh model applied to the proposed resolver with shorter length for the airgap and teeth is shown in Figure 10 as well.

The self-inductance of the excitation winding and the mutual inductance between excitations and signals of the proposed and conventional resolvers are affected by the narrowing of the excitation teeth. Figure 11 compares the two resolvers from the inductance perspective. The results indicate that narrowing the

FIGURE 8 | Output signals of the proposed model by MEC and harmonic Content. (a) Output signals and envelopes. (b) Harmonic orders and THD.
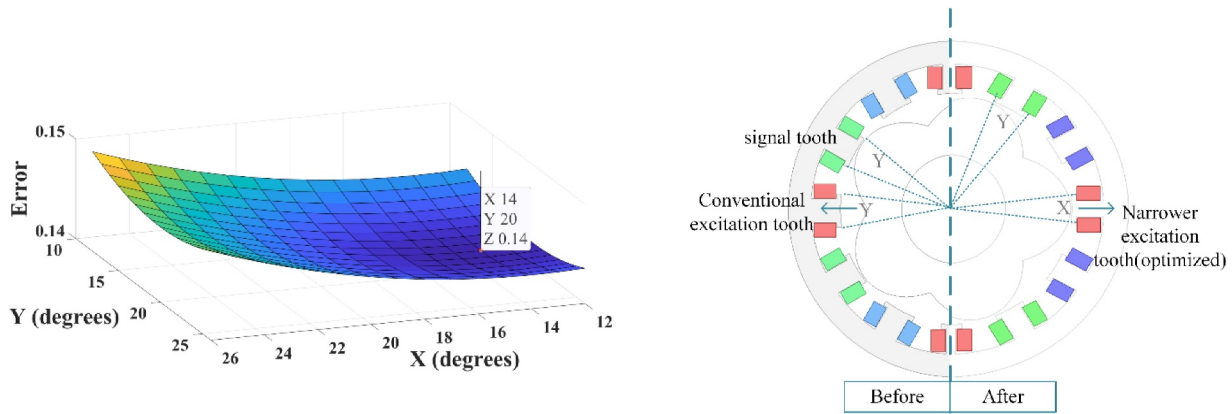
FIGURE 9 | FEM optimisation for the stator excitation and signal pitches.

TABLE 2 | Comparison between MEC and FEM simulation.

Parameter	FEM	MEC
Time step	1e-006 (s)	1e-006 (s)
Number of samples	25	25
Accuracy parameter	Mesh (airgap) = 0.1 Mesh (Resolver) = 1.5	Zones = 9 Nodes = 24
Simulation time	470 minutes	27 minutes
Optimisation method	SA	GA
MPE	0.138	0.14
AAPE	0.045	0.047

teeth reduces self-inductance of the excitation winding, whereas the mutual inductance between the excitation and signal windings remains almost unchanged.

Figure 12 illustrates the results of mutual inductance between excitation and signal windings calculated by FEM and MEC for the proposed model. It can be seen that there is negligible difference (62.4nH) between the results of the proposed MEC model and the FEM results. This validates the accuracy of the proposed MEC model.

Figure 13 provides a detailed comparison of the self-inductance of the proposed and conventional resolvers as calculated by both
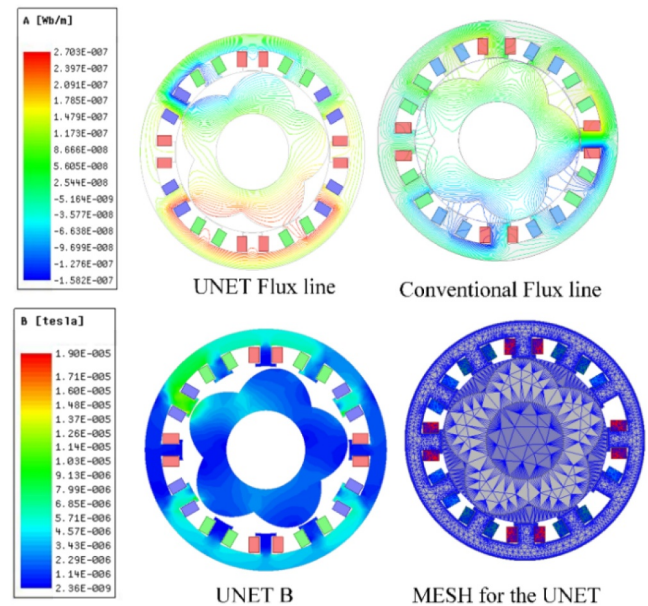

FIGURE 10 | Applied mesh, flux lines and field for the proposed resolver model.

FEM and MEC. The results show that the self-inductance of the excitation winding decreases from 6.81 to 5.66 mH in the proposed model. This reduction in self-inductance indicates that more flux lines circulate through the air gap, potentially
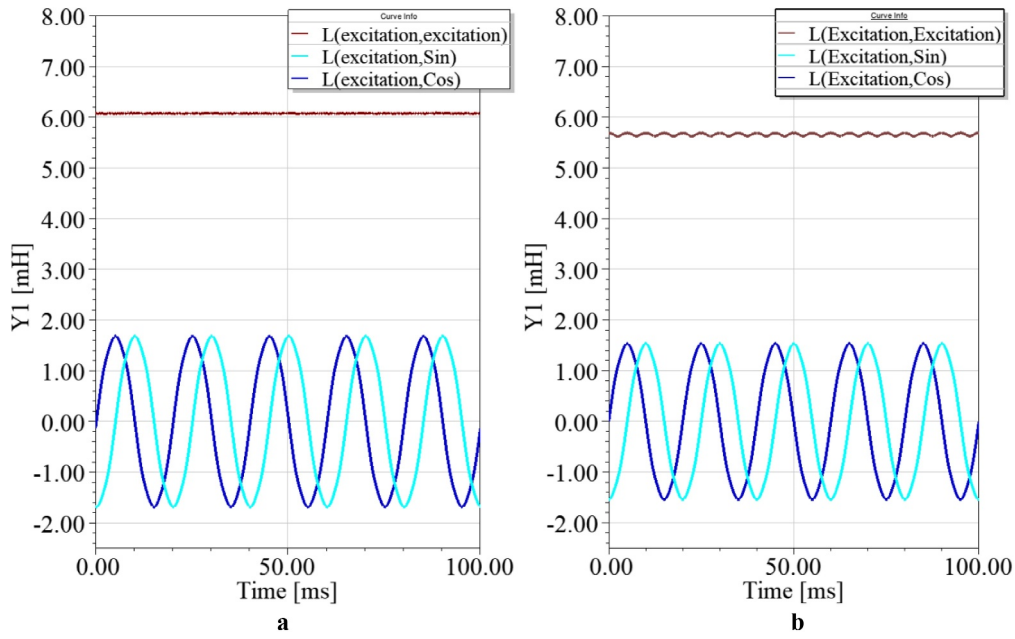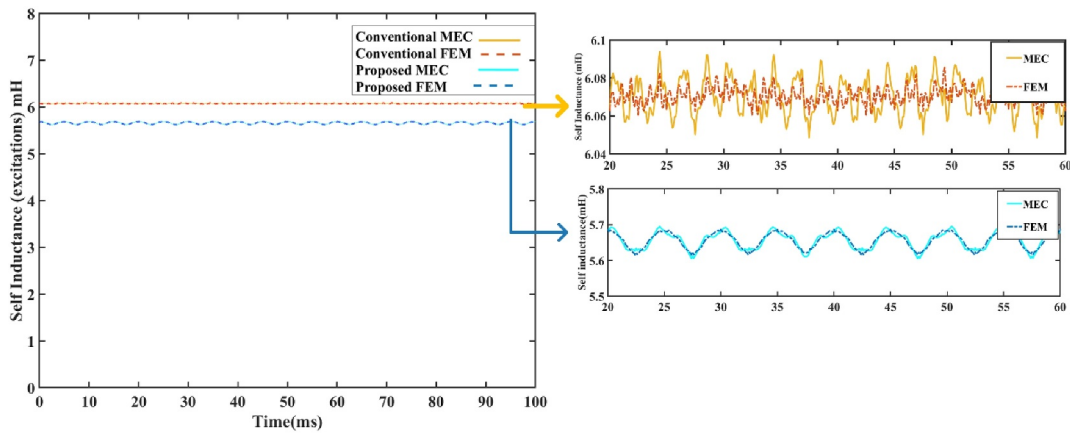
FIGURE 11 | Self-inductance and mutual inductances of the proposed and conventional models. (a) Conventional. (b) Proposed.
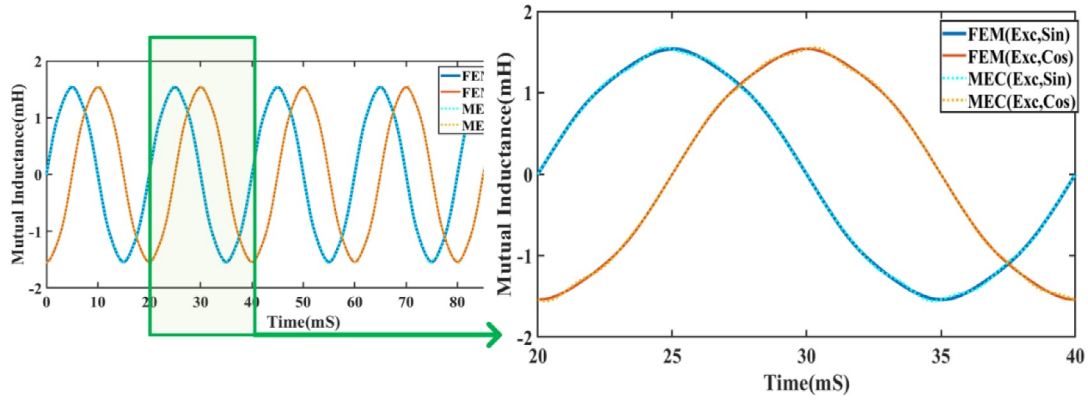
FIGURE 12 | Mutual inductance of the excitation and signal windings by MEC and FEM.

FIGURE 13 | Self-inductance of the proposed and conventional models by MEC and FEM.

enhancing sensitivity to rotor position and thereby reducing position error. Another notable difference between the proposed and conventional models is the variation in inductance which is higher in the proposed model. This increased variation reflects greater sensitivity to rotor reluctance changes, resulting in improved accuracy.

As it can be seen from Figures 12 and 13, the mutual and self-inductances are similar in both the MEC and FEM models. Therefore, the output signals and as a result the envelopes and the accuracy of both models will be similar. Thus, hereinafter the FEM model will be used to evaluate the performance of the proposed model.

5.2 | Performance of Proposed Resolver

The output waveform of the sine and cosine signals of the stator winding over one and a half full cycle of rotation is shown in Figure 14a. Figure 14b shows the zoomed-in view of the same output, highlighting the overlap between sin and cosine signals. Figure 14c depicts the excitation current.

Figure 15 shows the out envelope of sine and cosine winding. To obtain the envelopes of the sine and cosine windings, the Hilbert transform is used, and by taking the absolute value of the analytic signal, the envelope of the signal is determined. This

approach is advantageous for accurately demodulating signals as it preserves phase information while effectively filtering high-frequency signal. The resulting envelope provides a clean representation of the modulated signal. Based on the outputs of the Hilbert function, the proposed resolver exhibits a 0.013-degree improvement in resolver position detection compared to the conventional model.
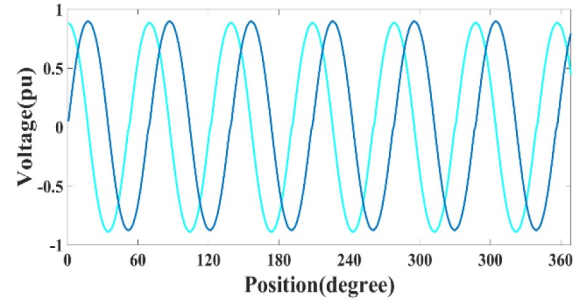

FIGURE 15 | Envelopes of signal windings in proposed resolver.
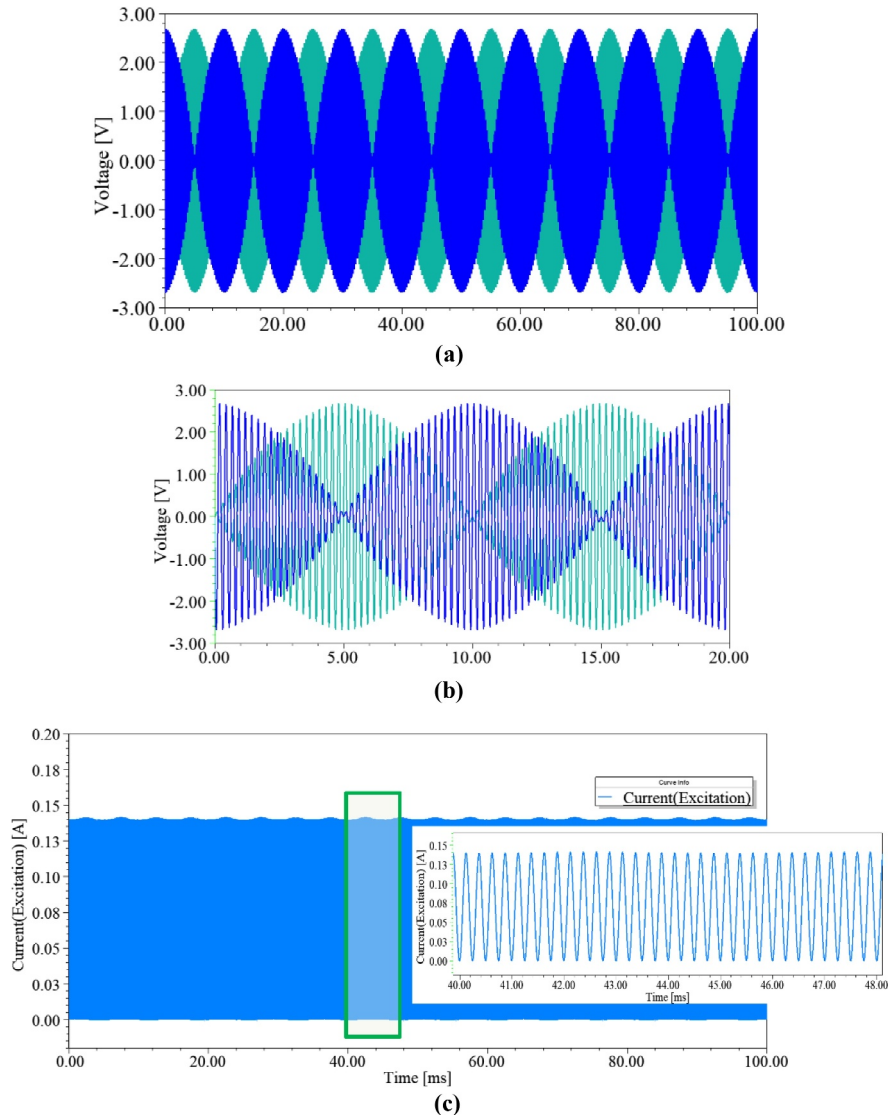

(a)

(b)

(c)

FIGURE 14 | Output of signal windings in proposed resolver. (a) Sine and cosine of the UNET resolver. (b) Zoomed signal for better visibility. (c) Excitation current.

Comparing the sinusoidal and cosine waveforms of the proposed resolver with the conventional resolver can be challenging. To enhance visual comparison, plotting both waveforms on a single graph is useful. Figure 16 displays the sine and cosine envelope functions and the FEM outputs for both resolvers. In Quadrant I, the high-pass sinusoidal and cosine functions are plotted together. In Quadrant II, the high-pass sinusoidal function is compared with the low-pass cosine function, whereas in Quadrant III, the symmetric counterpart is shown. Quadrant IV presents the low-pass sinusoidal and cosine functions side by side.

Figure 17A shows positions of the proposed and conventional resolvers. Based on the outputs by subtracting the actual value from the ideal value, Figure 17B is obtained in which the MPE of the resolver is 0.138°, and its AAPE value is 0.047°. This indicates that the maximum error reduced by 0.068° (49.2%), and the average error has improved by 0.013° (25.8%) compared to the conventional resolver.

5.3 | Performance Trade-off

Comparing the results of Figure 16 shows that the amplitude of the proposed resolver is lower than that of the conventional one. This is primarily because of the reduction in inductance of the proposed resolver as shown in Figure 13. The reduction in signal amplitude is 11% compared to the conventional resolver. However, this reduction in amplitude can be neglected as it has
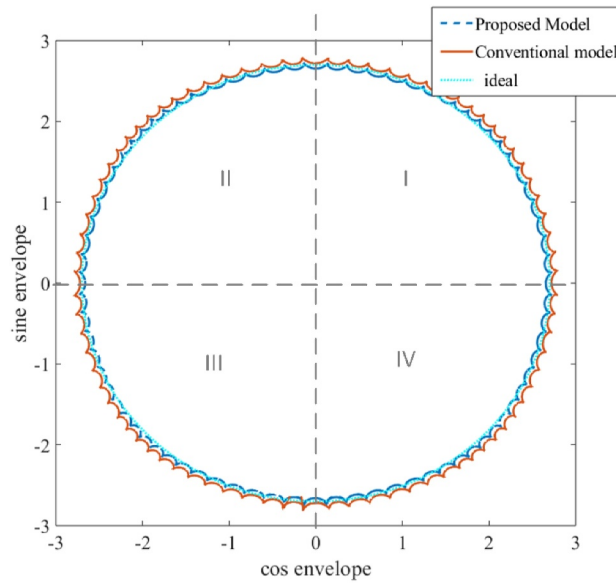
FIGURE 16 | Envelope output of signal windings in proposed resolver and signal windings outputs.
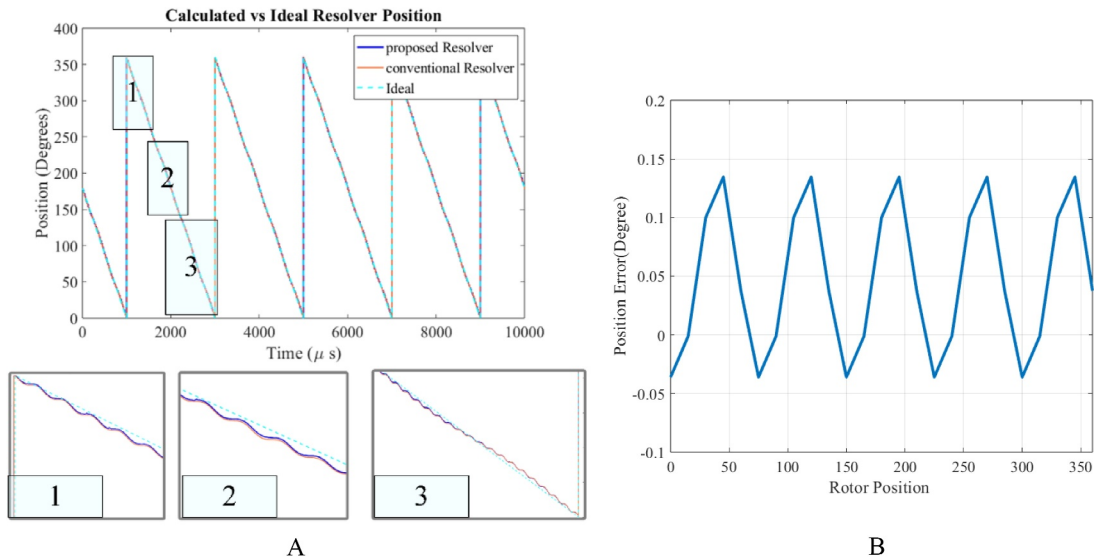
FIGURE 17 | Position of proposed resolver and position error. (A) Resolver position. (B) Position error.

a minor effect on the resolver's performance. The minimum amplitude voltage required for most RDC converters is between 2 and 5V, and the proposed model can provide sufficient amplitude within this range. Furthermore, the AAPE and MPE of the resolvers, which are key performance metrics, have improved. Therefore, the accuracy has increased at the expense of the signal amplitude.

6 | Experimental Results

The proposed optimised unequal teeth configuration was prototyped to validate the results of the simulation. Figure 18 shows the stator and rotor of the UNET configuration together with the stator after being coated by epoxy for safer winding process. Using epoxy instead of mylar paper also provides more space for winding and ensures symmetric winding. Four fins are included to simplify the assembly. A non-overlapping winding is used, and a case with a cap is designed to securely fix the resolver. The resolver is mounted on the shaft of a DC shunt motor. The test bench setup is shown in Figure 19.

According to Figure 18, the proposed stator has narrower excitation teeth which are 1.1 mm narrower than those of the
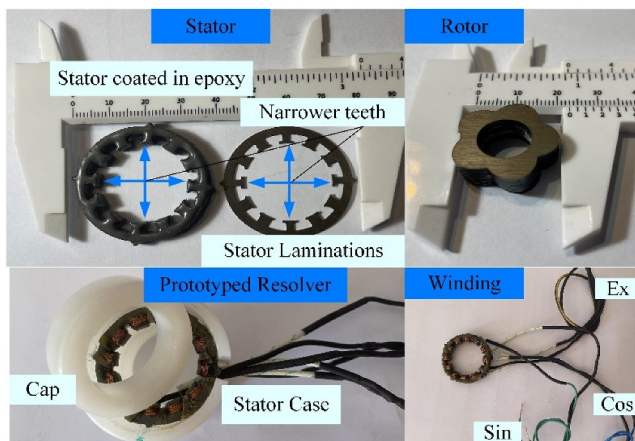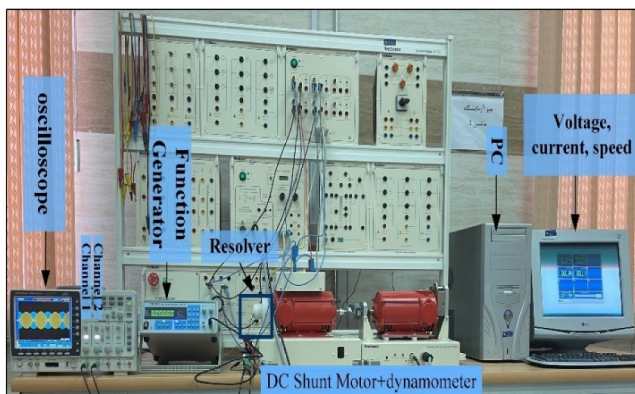

FIGURE 18 | Prototyped resolver.

FIGURE 19 | Test bench for the experimental test.

conventional model. Considering the accuracy and tolerance of the wire cutting machines, which is ± 0.001 mm, the same procedure can be applied in the manufacturing of the proposed model. The excitation winding is fed by 5-V 5-kHz sine waveform using the function generator as it is shown in Figure 20.

Both signal windings are connected to oscilloscope and output signals are displayed in Figure 21. In order to check the performance of the resolver in wide range of speeds, the resolver underwent under test at 300 and 800 rpm. The output signals of both channels together are shown to demonstrate the symmetric performance of the UNET resolver under 300 and 800 rpm.

In order to calculate the inherent error of the prototyped resolver, the set up with constant speed is controlled and the ideal position of the rotor is considered as the reference rotor position. Based on the experimental outputs, the MPE of the resolver is 0.148°, and its AAPE value is 0.0478° which are in close agreement with the simulation results. In order to check the amplitude accuracy of the resolvers, sine and cosine waveforms are plotted, similar to Figure 16, in Figure 22. The circular shape of the plot ensures the accuracy of the proposed model under both speeds.

Figure 23 compares the accuracy of the resolver by MEC, FEM and experimental results. Figure 23 shows that the experimental results are in close agreement (less than 8% difference) with the simulation results.

7 | Conclusion

In this article, a non-overlapping reluctance resolver featuring narrower excitation teeth in the stator is proposed and prototyped to enhance performance. First, a UNET configuration is applied to the stator using a non-overlapping winding method, and the effectiveness of this approach is investigated. Next, the size optimisation of the excitation teeth is explored using a MEC model with a detailed mathematical representation. The excitation teeth are modelled using three flux tubes and six segments for optimisation. Genetic algorithm is employed to determine the optimal dimensions of both the signal and excitation teeth while maintaining resolver symmetry. The proposed model is analysed to minimise error through FEM simulations. A comparison of flux lines and performance between the UNET
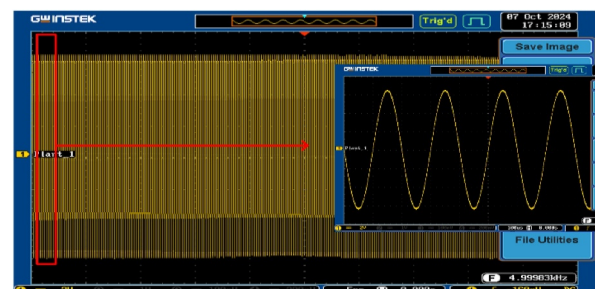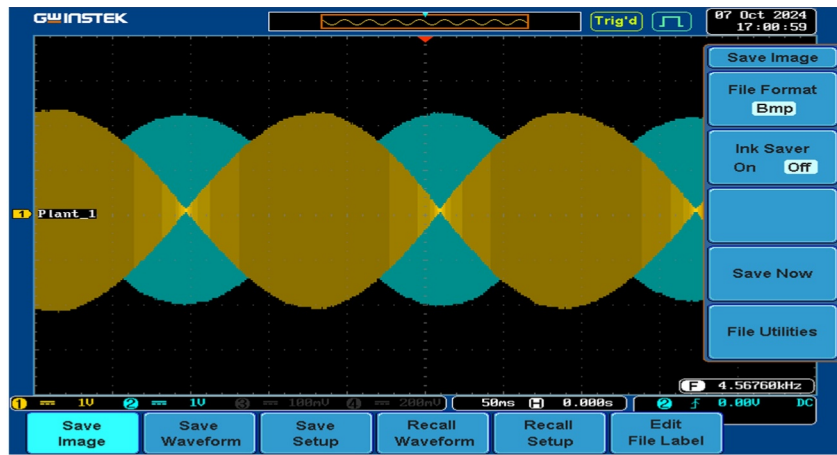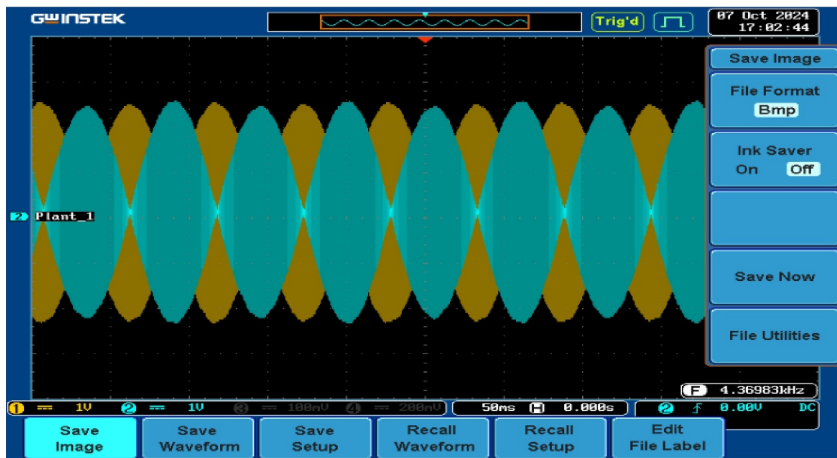

FIGURE 20 | Excitation signal with time. Div = 50 ms and 100 µs.

(a)

(b)

FIGURE 21 | Sine and cosine signals outputs. For 300 and 800 rpm. (a) Signal winding outputs (300 rpm, volt div. = 1 V and time div. = 50 ms) (see Figure 14b). (b) Sine and cosine windings from both channels (800 rpm, volt div. = 1 V and time div. = 50 ms) (see Figure 14a).

a: (time. div. = 50ms, volt. div.=2 v @300rpm)

b: (time. div. = 50ms, volt. div.=2 v @800rpm)
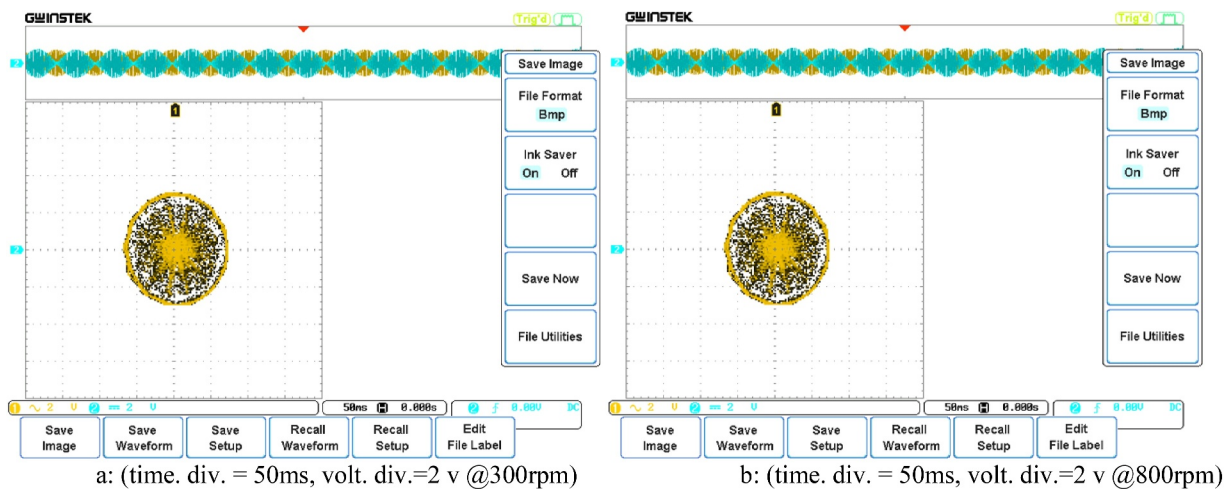
FIGURE 22 | Channel 1 (sine) versus channel 2 (cosine) plot.
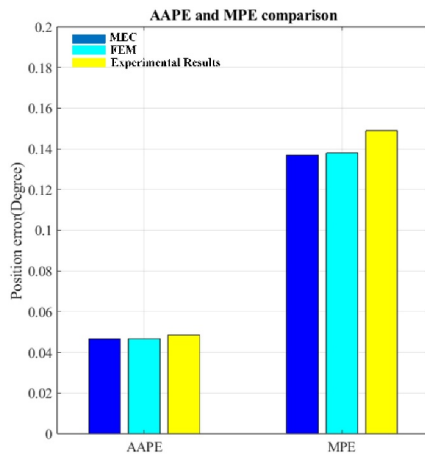
FIGURE 23 | AAPE and MPE comparison of MEC, FEM and experimental results.

and the conventional design is provided. It is shown that although the inductance of windings improved and higher accuracy obtained, the amplitude of the signal decreased insignificantly. Finally, the UNET resolver is prototyped, and experimental results validate the simulation findings. The comparison indicates that the maximum error reduced by 0.068° (49.2%), and the average error improved by 0.013° (25.8%).

Author Contributions

Davood Karamalian: conceptualization, formal analysis, investigation, software, validation, visualization, writing – original draft. **Behrooz Majidi:** conceptualization, data curation, investigation, validation. **Mohammadreza Moradian:** conceptualization, methodology, resources, supervision, validation, visualization. **Khoshnam Shojaei:** software, validation, writing – review and editing. **Sayyed Mohammad Mehdi Mirtalaei:** data curation, validation, writing – review and editing.

Acknowledgements

The authors have nothing to report.

Conflicts of Interest

The authors declare no conflicts of interest.

Data Availability Statement

The data that support the findings of this study are available from the corresponding author upon reasonable request.

References

1. F. Mashhadifarahani, A. Siadatan, D. Karamalian, B. Majidi, and A. Ghadimi, "Designing and Optimization of 9/12 Stator Permanent Magnet SRM to Improve Torque Ripple," in *2019 IEEE 28th International Symposium on Industrial Electronics (ISIE)* (2019), 290–295, https://doi.org/10.1109/ISIE.2019.8781341.

2. R. Setbacken, "System Performance and Application Tradeoffs Determine the Choice Between Encoders and Resolvers in Brushless Servos," *Powerconversion and Intelligent Motion-English Edition* 22, no. 5 (1996): 69–76.

3. L. Sun, J. Taylor, A. D. Callegaro, and A. Emadi, "Stator-PM-Based Variable Reluctance Resolver With Advantage of Motional Back-EMF," *IEEE Transactions on Industrial Electronics* 67, no. 11 (2020): 9790–9801, https://doi.org/10.1109/TIE.2019.2955410.

4. X. Ge, Z. Q. Zhu, R. Ren, and J. T. Chen, "Analysis of Windings in Variable Reluctance Resolver," *IEEE Transactions on Magnetics* 51, no. 5 (2014): 1–10, https://doi.org/10.1109/tmag.2014.2369993.

5. F. Tootoonchian and F. Zare, "Sinusoidal Area 2-DoF Variable Reluctance Resolver," *IEEE Sensors Journal* 24, no. 2 (2024): 1358–1365, https://doi.org/10.1109/JSEN.2023.3337276.

6. F. Tootoonchian and F. Zare, "A Tubular Variable Reluctance Resolver With Single Coil Excitation Winding," *IEEE Sensors Journal* 24, no. 3 (2024): 2657–2663, https://doi.org/10.1109/JSEN.2023.3342875.

7. F. Tootoonchian and Z. Nasiri-Gheidari, "Twelve-slot Two-Saliency Variable Reluctance Resolver With Non-overlapping Signal Windings and Axial Flux Excitation," *IET Electric Power Applications* 11, no. 1 (2017): 49–62, https://doi.org/10.1049/iet-epa.2016.0252.

8. H. Saneie, Z. Nasiri-Gheidari, and F. Tootoonchian, "Analytical Model for Performance Prediction of Linear Resolver," *IET Electric Power Applications* 11, no. 8 (2017): 1457–1465, https://doi.org/10.1049/iet-epa.2016.0693.

9. Z. Nasiri-Gheidari and F. Tootoonchian, "Influence of Mechanical Faults on the Position Error of an Axial Flux Brushless Resolver Without Rotor Windings," *IET Electric Power Applications* 11, no. 4 (2017): 613–621, https://doi.org/10.1049/iet-epa.2016.0675.

10. M. Emadaleslami, M. Khajueezadeh, and F. Tootoonchian, "Static Eccentricity Fault Location Diagnosis in Resolvers Using Siamese-Based Few-Shot Learning," *IEEE Transactions on Instrumentation and Measurement* 72 (2023): 1–9, https://doi.org/10.1109/tim.2023.3298404.

11. M. KhajueeZadeh and F. Tootoonchian, "Axial Flux Resolver Versus Radial Flux One From Fault Tolerability Point of View," *IEEE Sensors Journal* 23, no. 17 (2023): 19176–19183, https://doi.org/10.1109/JSEN.2023.3296746.

12. G. S. Moghaddam, Z. Nasiri-Gheidari, and R. Alipour-Sarabi, "Hybrid Excitation for a Wide Speed Range Linear Sinusoidal Area Variable Reluctance Resolver," *IEEE Transactions on Instrumentation and Measurement* 73 (2024): 1–7, https://doi.org/10.1109/TIM.2024.3406812.

13. R. Celikel, G. Boztas, and O. Aydogmus, "An Investigation on the Position Errors of Resolvers Designed in Different Structures: A Review," *Measurement* 218 (2023): 113186, https://doi.org/10.1016/j.measurement.2023.113186.

14. X. Ge, Z. Q. Zhu, R. Ren, and J. T. Chen, "A Novel Variable Reluctance Resolver for HEV/EV Applications," *IEEE Transactions on Industry Applications* 52, no. 4 (2016): 2872–2880, https://doi.org/10.1109/TIA.2016.2533600.

15. X. Ge, Z. Q. Zhu, R. Ren, and J. T. Chen, "A Novel Variable Reluctance Resolver With Nonoverlapping Tooth–Coil Windings," *IEEE Transactions on Energy Conversion* 30, no. 2 (2015): 784–794, https://doi.org/10.1109/TEC.2014.2377214.

16. A. Keyvannia, F. Zare, and F. Tootoonchian, "Analytical Modeling of Variable-Reluctance Tubular Resolver Based on Magnetic Equivalent Circuit and Conformal Mapping," *IEEE Transactions on Instrumentation and Measurement* 70 (2021): 1–8, https://doi.org/10.1109/tim.2021.3119141.

17. H. Saneie and Z. Nasiri-Gheidari, "Generalized Nonoverlapping Tooth Coil Winding Method for Variable Reluctance Resolvers," *IEEE Transactions on Industrial Electronics* 69, no. 5 (2021): 5325–5332, https://doi.org/10.1109/tie.2021.3084157.

18. R. Alipour-Sarabi, Z. Nasiri-Gheidari, F. Tootoonchian, and H. Oraee, "Analysis of Winding Configurations and Slot-Pole Combinations in Fractional-Slots Resolvers," *IEEE Sensors Journal* 17, no. 14 (2017): 4420–4428, https://doi.org/10.1109/JSEN.2017.2707523.

19. M. Bahari and F. Tootoonchian, "Performance Analysis of an Outer Rotor Variable Reluctance Resolver," *IEEE Sensors Journal* 22, no. 18 (2022): 17761–17768, https://doi.org/10.1109/JSEN.2022.3195728.

20. L. Sun, J. Taylor, A. D. Callegaro, and A. Emadi, "Stator-PM-based Variable Reluctance Resolver With Advantage of Motional Back-EMF," *IEEE Transactions on Industrial Electronics* 67, no. 11 (2019): 9790–9801, https://doi.org/10.1109/tie.2019.2955410.

21. L. Sun, Z. Luo, K. Wang, R. Cao, and S. Ding, "A Stator-PM Resolver With Field Modulation Principle," *IEEE Transactions on Energy Conversion* 36, no. 1 (2020): 159–172, https://doi.org/10.1109/tec.2020.3001655.

22. L. Sun, Z. Luo, J. Hang, S. Ding, and W. Wang, "A Slotless PM Variable Reluctance Resolver With Axial Magnetic Field," *IEEE Transactions on Industrial Electronics* 69, no. 6 (2022): 6329–6340, https://doi.org/10.1109/TIE.2021.3090704.

23. X. Ge and Z. Q. Zhu, "A Novel Design of Rotor Contour for Variable Reluctance Resolver by Injecting Auxiliary Air-Gap Permeance Harmonics," *IEEE Transactions on Energy Conversion* 31, no. 1 (2016): 345–353, https://doi.org/10.1109/TEC.2015.2470546.

24. A. E. Hoffer, I. Petrov, J. J. Pyrhönen, J. A. Tapia, and G. Bramerdorfer, "Analysis of a Tooth-Coil Winding Permanent-Magnet Synchronous Machine With an Unequal Teeth Width," *IEEE Access* 8 (2020): 71512–71524, https://doi.org/10.1109/ACCESS.2020.2987872.

25. G. J. Li and Z. Q. Zhu, "Analytical Modeling of Modular and Unequal Tooth Width Surface-Mounted Permanent Magnet Machines," *IEEE Transactions on Magnetics* 51, no. 9 (2015): 1–9, https://doi.org/10.1109/TMAG.2015.2432735.

26. G. Liu, R. Guan, and L. Xu, "Unequal Stator Modulated Teeth Structure to Reduce Electromagnetic Vibration in Permanent Magnet Vernier Machine," *IEEE Transactions on Industrial Electronics* 70, no. 12 (2023): 12036–12047, https://doi.org/10.1109/TIE.2023.3239778.

27. R. Ghandehari, P. Naderi, and L. Vandevelde, "Performance Analysis of a New Type PM-Resolver in Healthy and Eccentric Cases by an Improved Parametric MEC Method," *IEEE Transactions on Instrumentation and Measurement* 70 (2021): 1–10, https://doi.org/10.1109/TIM.2021.3080388.

28. P. Naderi, R. Ghandehari, and M. Heidary, "A Comprehensive Analysis on the Healthy and Faulty Two Types Vr-Resolvers With Eccentricity and Inter-turn Faults," *IEEE Transactions on Energy Conversion* 36, no. 4 (2021): 3502–3511, https://doi.org/10.1109/tec.2021.3079725.

29. P. Naderi, "A Novel Variable-Reluctance Resolver Proposal and its Performance Analysis under Healthy and Eccentric Cases," *Mechatronics* 90 (2023): 102948, https://doi.org/10.1016/j.mechatronics.2023.102948.

30. H. Saneie, Z. Nasiri-Gheidari, and F. Tootoonchian, "Design-Oriented Modelling of Axial-Flux Variable-Reluctance Resolver Based on Magnetic Equivalent Circuits and Schwarz–Christoffel Mapping," *IEEE Transactions on Industrial Electronics* 65, no. 5 (2018): 4322–4330, https://doi.org/10.1109/TIE.2017.2760862.